Review of Scientific Instruments

RESEARCH ARTICLE | NOVEMBER 08 2024

Demonstration of a container-less method for investigating high-temperature alloy properties using ED-XRD

Frank McKay ; Kane Bergeron; Amitava Roy ; S. Thomas Britt ; Michael P. SanSoucie ; Brandon S. Phillips; Jonathan Raush ; Phillip T. Sprunger

Check for updates

Rev. Sci. Instrum. 95, 113902 (2024)
https://doi.org/10.1063/5.0213480
CHORUS

View Online
Export Citation

Articles You May Be Interested In

A new compact symmetric shear diamond anvil cell for *in situ* high-pressure-torsion studies

Rev. Sci. Instrum. (May 2024)

Evaluation of morphology and crystallinity of biaxially oriented polypropylene films

AIP Conf. Proc. (February 2019)

High-performance thermoelectric mineral $Cu_{12-x}Ni_xSb_4S_{13}$ tetrahedrite

J. Appl. Phys. (January 2013)

03 April 2025 13:33:43

AIP Publishing

Review of Scientific Instruments ARTICLE pubs.aip.org/aip/rsi

Demonstration of a container-less method for investigating high-temperature alloy properties using ED-XRD

Cite as: Rev. Sci. Instrum. 95, 113902 (2024); doi: 10.1063/5.0213480
Submitted: 10 April 2024 • Accepted: 14 October 2024 •
Published Online: 8 November 2024

View Online Export Citation CrossMark

Frank McKay,[1] Kane Bergeron,[2] Amitava Roy,[3] S. Thomas Britt,[4] Michael P. SanSoucie,[5] Brandon S. Phillips,[5] Jonathan Raush,[2] and Phillip T. Sprunger[1,3,a)]

AFFILIATIONS

[1] Department of Physics and Astronomy, Louisiana State University, Baton Rouge, Louisiana 70803, USA
[2] Department of Mechanical Engineering, University of Louisiana at Lafayette, Lafayette, Louisiana 70504, USA
[3] Center for Advanced Microstructures and Devices, Louisiana State University, Baton Rouge, Louisiana 70803, USA
[4] Jacobs Space Exploration Group, 620 Discovery Dr NW, Huntsville, Alabama 35806, USA
[5] NASA Marshall Space Flight Center, Huntsville, Alabama 35812, USA

[a)] **Author to whom correspondence should be addressed:** phils@lsu.edu

03 April 2025 13:33:43

ABSTRACT

As new alloys are being developed for additive manufacturing (AM) applications, questions related to the temperature-dependent structural and compositional stability of these alloys remain. In this work, the benefits and limitations of a unique method for testing this stability are presented. This system employs the use of polychromatic synchrotron light to perform energy-dispersive x-ray diffraction (ED-XRD) on an electrostatically levitated sample at high temperatures. In comparison with a traditional angular-dispersive setup, the container-less electrostatic levitation method has unique advantages, including quicker acquisition times, simultaneous compositional information through fluorescence emissions, a reduction in background noise, and, importantly, concurrent/subsequent measurement of thermophysical properties. This combined method is ideal for phase transition studies by holding the levitated sample at a stable position and temperature through controlled heating and temperature management. To illustrate these capabilities, we show ED-XRD data of the well-known martensitic phase transition (hcp to bcc) in Ti–6Al–4V. In addition, results from the novel alloy $Ni_{51}Cu_{44}Cr_5$ are presented. This alloy is shown to maintain an fcc structure upon heating. However, the concentration of Cu is reduced at high temperatures, resulting in a decrease in the lattice constant. As concurrent thermophysical properties are probed, these preliminary structure and composition experiments demonstrate the capabilities of this technique to determine the composition–processing–structure–properties of metal alloys for AM.

Published under an exclusive license by AIP Publishing. https://doi.org/10.1063/5.0213480

I. INTRODUCTION

Additive manufacturing (AM) of metal alloys has a variety of beneficial uses, such as rapid prototyping, manufacturing of geometries not possible with other methods, and creation of parts with difficult to machine alloys. However, a major challenge of developing new metal alloys for use in AM is determining if the desired properties of these alloys can be maintained during the high temperatures and rapid solidification associated with AM processes. Many materials properties such as hardness and ductility, along with other mechanical and electrochemical properties, are tied to the long- and short-range structural details of an alloy. When alloys are melted, or even just heated, they can form different structures and compositions upon cooling, which can lead to a change in their properties.

While there are many different techniques for AM of metal alloy parts,[1] all require exposure to high temperatures. In a powder bed fusion process,[2] a solid metal powder is liquefied by a laser and then rapidly re-solidified. Friction stir additive manufacturing[3] rapidly rotates a solid or powder feedstock, heating it to near 80% of its melting point, causing it to plastically deform onto the build surface. These processes can be problematic for many alloys that contain elements that vaporize easily and can be preferentially lost during AM.[4,5]

Published under an exclusive license by AIP Publishing

In the past, electrostatic levitation (ESL) has been used extensively[6] for the measurement of thermophysical properties such as density, thermal expansion, surface tension, viscosity, emissivity, electrical conductivity, and vapor pressure.[7–16] Furthermore, a considerable amount of effort has been focused on analyzing the structural changes of materials with x-ray scattering and neutron scattering techniques using ESL.[17–22] The new experimental capabilities presented here expand upon those previous studies by combining the technique of energy-dispersive x-ray diffraction (ED-XRD)[23] with the simultaneous measurement of x-ray fluorescence (XRF) emissions. These new experimental capabilities, which involve a coupling between NASA Marshall Space Flight Center's (MSFC) mobile Electrostatic Levitation (ESL) Chamber[24] and LSU's synchrotron facility [(Center for Advanced Microstructures and Devices (CAMD)], help us answer critical questions about the structural and compositional stability, as well as thermophysical properties, of complex concentrated alloys used in AM processes. In this paper, we will show the preliminary results of these experiments and demonstrate some of the capabilities of this experimental setup.

II. BACKGROUND

Information about the crystal structure of a sample, such as a metal alloy, can be obtained by observing the elastic scattering of x rays. To measure this scattering, two techniques are generally available. The most common method is to use a monochromatic x-ray beam and perform angular scans [angular-dispersive x-ray diffraction (AD-XRD)]. An alternative method consists of employing a continuous (polychromatic) source of x rays, such as from a synchrotron. This latter ED-XRD technique uses an energy-sensitive detector to measure the elastically scattered x rays at a fixed angle. In ED-XRD, a modified version of Bragg's law is used,

$$E = \frac{hc}{2d\,\sin\theta}, \tag{1}$$

where E is the energy of the scattered x rays, d is the lattice spacing, θ is the fixed angle of the detector, and hc (1239.9 eV nm) is a constant. Apart from concurrent thermophysical property measurements, this method of combining ED-XRD with ESL has several advantages over a typical AD-XRD setup, which are listed as follows:[25,26]

- *Reduced acquisition time*: Since the detector does not have to move, the entire measurable spectrum can be acquired at the same time. In an angular setup, the scan time is limited by the angular speed of the diffractometer arms.
- *Steady experimental setup*: Once the sample is in its final position, the trajectory of the beam is fixed. Unlike in AD-XRD, no detector movement can compromise the alignment causing additional systematic error. In addition, small samples, or complex devices, such as heaters, can be easily introduced into the experimental setup. The beam must only be collimated down to just slightly larger than the sample size.
- *Simultaneous compositional information*: The relative composition of the sample components can be acquired simultaneously with structural information through the measurement of x-ray fluorescence (XRF) emission.
- These advantages make ED-XRD ideally suited for studies of phase transitions. However, some disadvantages need to be considered as follows:
- *Limitation of measurable energies*: The energy that can be measured is limited by the type of detector used. At a specific angle, this limits the value of d, or lattice spacing that can be measured. For our measurements with a Si drift detector (max = 20 keV) with $2\theta = 32.098°$, the range of d is limited to 1.12–4.48 Å.
- *Decrease in the lattice spacing resolution*: Using the modified Bragg's law, we can estimate the error in the lattice spacing[27] as $\delta d/d = 0.002$. This error consists of two parts: one from the energy resolution of the detector and the other from the angular divergence of the outgoing x-ray beam. The energy resolution is fixed, but given sufficient flux, the angular divergence can be improved with collimation of the outgoing x rays.
- *Varying probing depth*: The probing depth, or penetration depth of the x rays, is dependent on the energy of the x rays and the mass adsorption coefficient of the sample through the Lambert–Beer law. For any sample, given its density and energy of each XRF emission/scattering peak, the probing depth can vary by several microns. For example, if a pure Cr sample with K_α emission at 5.4 keV is considered,[28] then the attenuation length of the x rays would be (given our experimental setup) 8.8 μm.[29] However, in the case of a pure Cu sample with K_α emission at 8.0 keV,[28] the attenuation length of the x rays would be 11.8 μm.[29]

The last disadvantage leads to a unique issue with the measurement of the depth-dependent compositional change in the sample. Upon synchrotron white-light illumination, the total flux of photons that could cause XRF emissions can differ depending on their respective energy. The majority of the incident light on the sample will have a much higher energy than required for fluorescence emission and will penetrate deep into the sample. However, the characteristic emission from the interior of the sample may not make it all the way out of the sample depending on the mass absorption coefficient. Each emission will be attenuated differently.

The intrinsic photon energy spectrum from the synchrotron insertion device is modified through interactions with anything between the synchrotron and the sample, such as collimators, filters, windows, and any air in between the beamline and sample as illustrated in Fig. 1 (red line). A simulation of the incoming photon flux from the CAMD synchrotron at the wavelength-shifter x ray diffraction (WXRD) beamline is shown in Fig. 1 (black line). This spectrum was generated using the software x-ray oriented programs (XOP),[30] using the appropriate filters (for x-ray absorbers) for our experimental setup, which consisted of a 0.3 mm Be window, a 0.3 mm Al window, and a 150 mm air gap (N_2). This representation also considers the operating parameters for the wavelength shifter[31] spectrum during our experiments, which were a magnetic field of 6.5 T and a beam energy of 1.1 GeV.

Despite this classification of the incoming spectrum, it does not fully account for all the issues related to XRF elemental quantification. Additional effects can alter the intensity of measured XRF emissions, including extra x-ray absorbers beyond the sample and secondary excitations from other components' XRF emissions.

03 April 2025 13:33:43

Published under an exclusive license by AIP Publishing

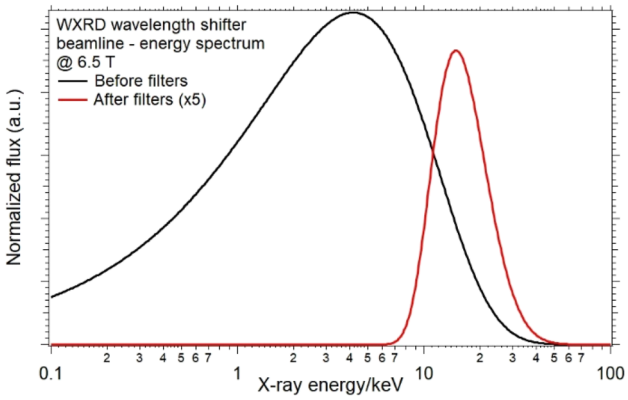

FIG. 1. Energy spectrum of x rays exiting the CAMD beamline operating at 6.5 T with a beam energy of 1.1 GeV. The black line represents the overall x-ray spectra, and the red line represents the spectrum after filters (for x-ray absorbers).

However, precise quantification is primarily limited by the density-dependent attenuation length of the x-ray emissions. Since density is determined by composition, a comparison with known standards is necessary to determine the appropriate correction factors for accurate quantification. A comprehensive analysis of these factors and comparison with well-established standards is beyond the current scope of this study. Nonetheless, these factors are not temperature dependent. This means that the relative change in the XRF intensity as a function of temperature can indicate compositional changes in the near-surface region (<15 μm). This requires normalizing the spectrum for factors affecting intensity between measurements, such as synchrotron beam current and acquisition time.

Finally, the thermophysical property measurements afforded by this technique allow for the ability to bring a sample all the way to its melting point, while probing the sample's density, thermal expansion,[8] and surface tension[11] simultaneously with structural measurements. These results can be critical for implementation in AM applications.[32,33]

III. EXPERIMENTAL SETUP

Our experimental setup combined the advantages of ED-XRD with the additional benefits of container-less processing, specifically with the use of ESL. This combination allowed us to collect thermophysical property data and process samples with a significant reduction in background signal and artifacts. In addition, no interfacial interactions with a holder were possible, since the sample was under vacuum (~10^{-7} Torr) and not in any physical contact with any other materials while being heated.

A schematic of our ED-XRD experimental setup is shown in Fig. 2(a). The vacuum chamber was connected to CAMD's WXRD wavelength shifter beamline, providing white light out of the beamline with an energy spectrum as shown in Fig. 1. The CAMD synchrotron and ESL chamber were separate vacuum systems, with a small (150 mm) air gap between them. The end of the CAMD beamline was sealed with an Al window (0.3 mm thick).

Prior to entering the chamber, the white light passed through a 4-jaw slit to cut the beam down to ~3 × 3 mm^2. With the synchrotron source located 21 m away, this resulted in a horizontal angular divergence of 0.14 mrad. The light then passed through a beryllium window (0.3 mm thick) before interacting with the levitated sample in the center of the ESL chamber. All XRF emissions and elastically scattered x rays [Eq. (1)], within the limited d-range, are measured at a fixed angle of 32.098° after passing through another beryllium exit window. Collimated through a combination of slits, a KETEK™ AXAS-M1 Si drift detector, which is sensitive to energies up to 20 keV, was used. This collimation was achieved by two methods: a horizontally oriented 2-jaw slit that reduced the beam down to ~1.5 mm in height and a vertically oriented series of twenty parallel tungsten sheets spaced about 0.5 mm apart. By measuring the x ray scattering and fluorescence from pure element samples of Ti, Cr, Fe, Co, Ni, and Zr at room temperature (RT ~25 °C), the detector

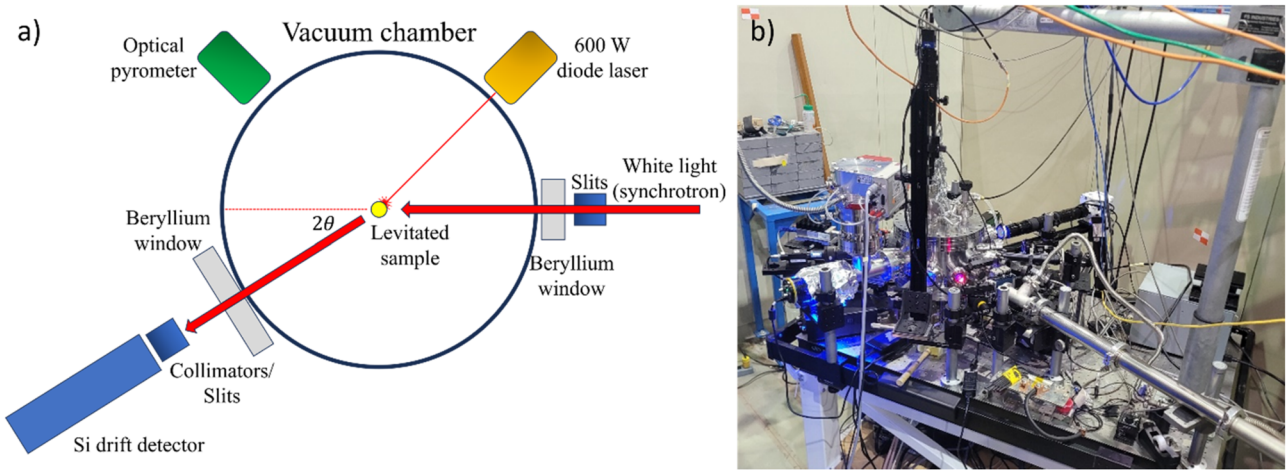

FIG. 2. (a) Schematic of the ED-XRD setup as connected at the CAMD synchrotron. (b) Image of the ESL chamber as installed at the WXRD beamline at CAMD.

03 April 2025 13:33:43

Published under an exclusive license by AIP Publishing

energy and angle were calibrated as described in the supplementary material.

All samples were spherical metal beads, about 2 mm in diameter. These samples were electrostatically levitated using a set of dynamically controlled electrodes as described by Rulison *et al.*[34] and others.[17,24] The capabilities of MSFC's ESL system are described in detail elsewhere,[17] but some slight distinctions should be noted. The charge compensation for the levitated sample, which is primarily provided by a UV source, is supplemented by x rays from the synchrotron, providing additional charge via the photoelectric effect. This could cause a destabilizing effect when the sample was initially launched into the electrostatic field but did not affect the samples' stability afterward. The ionization actually improved the stability of some samples, which were only able to be levitated to the melting point with the synchrotron radiation. During measurements, samples would rotate due to fluctuations in surface charge, but the sample's position remained fixed (within 100 μm) in the ~3 × 3 mm^2 area of incoming xrays. Once levitated, the sample could be heated with a 600 W 810 nm diode laser, and the temperature was monitored using an Impac IGA 140 optical pyrometer (300° to 2000 °C). Each measurement was taken once the sample had reached a stable temperature and position, with data recorded over a period of 180 s.

The samples, exposed to polychromatic light from the synchrotron, generated x ray scattering and XRF emissions, which provided structural and compositional information. Each sample was measured at a variety of temperatures from room temperature (RT, ~25 °C) to near its predicted melting point. In some cases, samples were measured at their melting point. All reported values of temperature were determined by averaging the temperature values recorded by the optical pyrometer during the time of measurement. It should be noted that evaporative losses due to preferential surface sublimation in ESL processing at high temperatures can be a significant factor[35,36] when dealing with multi-component alloys such as those presented here. In particular, certain thermophysical properties, for example surface tension, depend critically on the composition of the near-surface region.

These samples were made by mixing the desired concentrations of pure powders (99.99%) and arc-melting in an argon atmosphere on a water-cooled copper hearth with a tungsten electrode. The larger ingot was turned over several times and re-melted to ensure a homogeneous sample. A small piece was then cut off from the larger ingot, which was then arc-melted again to form a small (~2 mm) spherical metal bead, which is typical for processing in ESL applications.

In addition to structural and compositional scans, samples that were able to achieve a full melt cycle were processed for high temperature density measurements and thermal data. This was performed through the utilization of an ultrahigh speed camera and a radiation pyrometer, which are normal components of MSFC's ESL processing. In this case, when combined and synced through software analysis, these instruments allow for the determination of a material's temperature dependent density up to and through a material's liquidus, including superheated and undercooled regions. The measurements are performed by triggering a video of the sample in its levitated state once molten at a frame rate of 1000 fps. Upon triggering, the heating power supplied via laser is removed, and the sample is allowed to cool. This allows for the collection of the sample's change in diameter in pixels with respect to temperature as well as generating a temperature curve for the identification of liquidus, solidus, and undercooling potential. A video of a machined calibration sphere collected preprocess and the post-image analysis software allow for the conversion of the digital image into a measurement of the sample's 2D area and diameter in mm and therefore can produce usable volume measurements. Assuming a linear rate of material evaporation, pre- and post-processing mass values and volume measurements can be used in a general density formula to produce temperature dependent density relations throughout a sample's cooling cycle. The ability to generate these data simultaneously further emphasizes the novelty of this method.

IV. PRELIMINARY RESULTS

As a proof-of-concept for measuring phase transitions, we conducted scattering experiments on a well-known alloy, Ti–6Al–4V, which has been studied by other groups[37,38] for AM applications. According to CALculation of PHAse Diagram (CALPHAD) methods[39] and literature,[40,41] Ti–6Al–4V forms a hexagonal-close-packed (hcp) structure at RT, undergoes a martensitic phase transition to body-centered cubic (bcc) around 800 °C, and fully transitions at ~1000 °C. A 2 mm sample of Ti–6Al–4V was loaded into the ESL chamber, and measurements were taken at regular temperature increments. In Fig. 3, this structural phase transition is clearly revealed. At RT [Fig. 3(a), black line], the sample exhibits the expected single-phase hcp crystal structure. This structure persists until 959 °C (blue line), where the sample shows the predicted mix of hcp + bcc phases. Eventually, at 1002 °C (red line), all traces of an hcp structure are attenuated and the spectra are dominated by the scattering of a pure bcc structural phase.

In addition to Ti–6Al–4V, we conducted measurements of several 3D transition metal alloys, including $Ni_{51}Cu_{44}Cr_5$ from RT to 1389 °C. Ni- and Cu-based alloys have recently garnered interest for AM due to their excellent electrochemical and mechanical properties, as well as their applications in aerospace, oil, and gas industries.[42,43] This particular composition was chosen because it best illustrates the capabilities of this technique. The results of these measurements are shown in Fig. 4. Figure 4(a) shows the characteristic K_α and K_β emissions from Cr (5.4 and 5.9 keV), Ni (7.5 and 8.3 keV), and Cu (8.0 and 8.9 keV).[28] By integrating the contributions from each of these emission lines, we compared the elemental composition in the near-surface region (3–13 μm).[29] As mentioned before, it is only possible to quantify the relative change in composition as a function of temperature. After heating the sample, the relative intensity of the Cu XRF peaks decreased rapidly around 1100 °C [Fig. 4(a), top inset]. This decrease is understood to be primarily due to the much higher vapor pressure of Cu,[44] as compared to Ni,[45] resulting in a preferential evaporative loss from the near-surface region (probing depth) when approaching the melting point. This indicates that the sample is not compositionally stable in the near-surface region upon heating and melting.

This alloy forms a face-centered-cubic (fcc) structure [Fig. 4(b)], with the first three diffraction peaks labeled (111), (200), and (220) persisting up to 1389 °C. By fitting these three peaks for each temperature (as explained in the supplementary material), we can determine the average lattice constant [Fig. 4(c)]. This lattice constant increases as expected under thermal expansion

03 April 2025 13:33:43

Published under an exclusive license by AIP Publishing

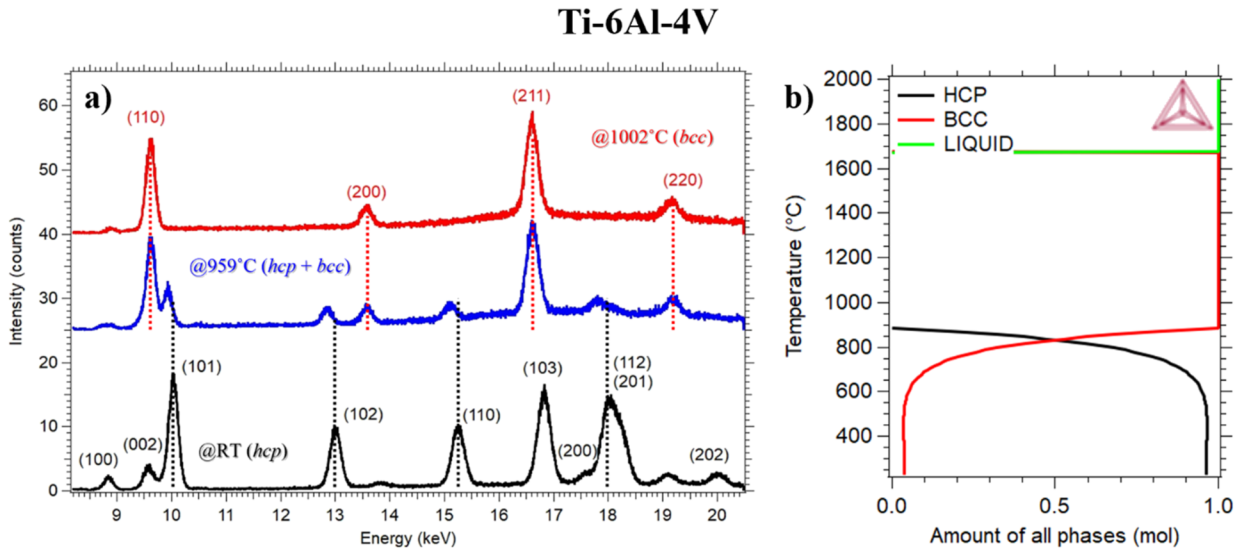

FIG. 3. (a) ED-XRD of Ti–6Al–4V alloy at RT (black), 959 °C (blue), and 1002 °C (red). The black dotted lines indicate the peaks of an hcp structure that appear at both RT and 959 °C. Note: As expected, a significant shift of hcp peaks is seen due to thermal expansion. The red dotted lines indicate the peaks of the bcc structure at both 959 and 1002 °C (b) Ti–6Al–4V phase diagram from CALPHAD showing a phase transition starting at around 800 °C.

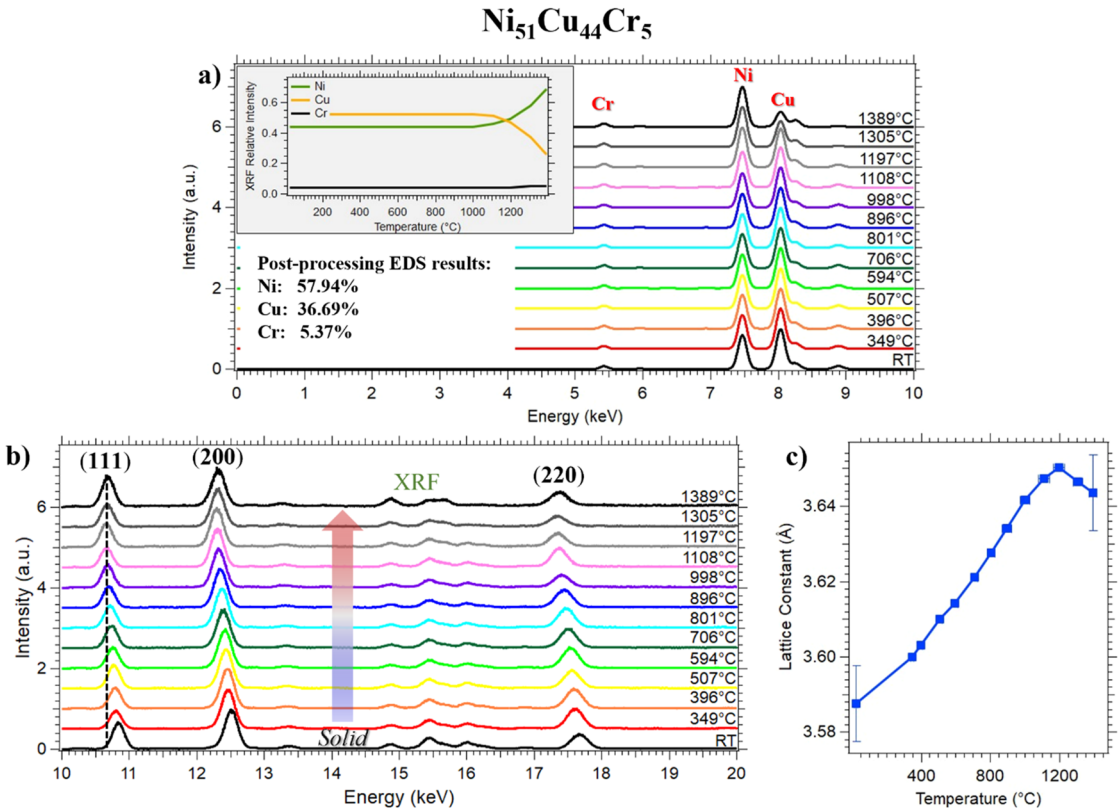

FIG. 4. (a) K_α and K_β fluorescence peaks from Cr, Ni, and Cu. Top inset: relative change in sample composition in the near-surface region at various temperatures. Bottom inset: composition determined by EDS post-processing. (b) X-ray scattering of the $Ni_{51}Cu_{44}Cr_5$ alloy showing (111), (200), and (220) peaks of an fcc structure. The black dashed line indicates the location of the (111) peak at 1389 °C, revealing thermal expansion of the sample. (c) Lattice constant determined from the fitting of (111), (200), and (220) peaks of the $Ni_{51}Cu_{44}Cr_5$ alloy in blue. Error bars displayed are typical for all data points.

03 April 2025 13:33:43

Published under an exclusive license by AIP Publishing

until 1100 °C, at which point it starts to decrease. From a Vegard's law[46,47] perspective, this is unsurprising. While Vegard's law does not generally apply very well to ternary systems,[48] the decrease in lattice constant happens at the same point as the decrease in Cu concentration [Fig. 4(a)]. Since pure Cu has a larger lattice constant (3.6149 Å)[49] than Ni (3.524 Å),[49] this is to be expected.

After performing these ED-XRD measurements, energy-dispersive x-ray spectroscopy (EDS) measurements were performed using a FEI Quanta 3D FEG Dual Beam FIB-SEM at the Shared Instrumentation Facility at Louisiana State University. Prior to EDS measurements, the sample was sanded and polished to half its diameter. EDS elemental quantification was performed in a $15 \times 15\ \mu m^2$ area within 5–10 μm of the edge, in a $15 \times 15\ \mu m^2$ area in the center of the sample, and across the entire 2 mm diameter. The compositions measured through EDS in all three regions did not differ significantly, so the reported compositions are results from the entire cross section (2 mm diameter) of the sample. This revealed (Fig. 4, bottom inset) a change in composition from $Ni_{51}Cu_{44}Cr_5$ to $Ni_{57.9}Cu_{36.7}Cr_{5.4}$, consistent with the decrease in Cu concentration observed in XRF.

In addition to compositional scan data produced for 3D transitional metal alloys, high temperature density and thermal cycle data were taken for the $Ni_{51}Cu_{44}Cr_5$ alloy. This resulted in the development of equations that characterize the relationship between the density of the material and temperature of the sample in regions above 1100 °C. The results from these data as well as a representation of the temperature of the sample through a melt cycle are shown in Fig. 5.

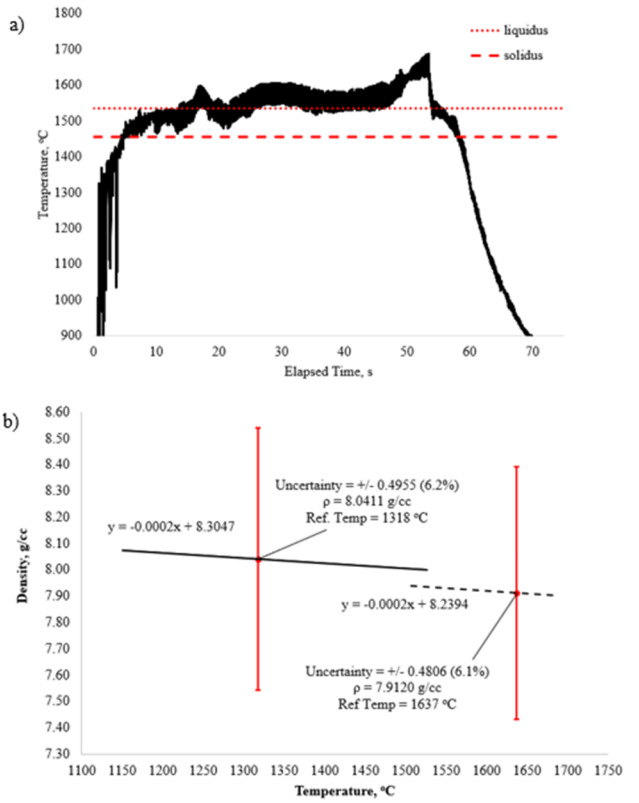

FIG. 5. (a) Melt profile from a typical ESL process displaying temperature characteristics, including the liquidus and solidus, respectively, of the sample processed. (b) Density vs temperature trends of the $Ni_{51}Cu_{44}Cr_5$ alloy in the solid and liquid regions of the material with respective characteristic uncertainties and equations noted.

In Fig. 5(a), the melt cycle presented has three distinct locations of interest being the beginning and exit temperatures of the melt plateau of the material and the degree at which the material undercooled. For the $Ni_{51}Cu_{44}Cr_5$ sample that was tested here, the respective solidus and liquidus temperatures were found to be 1455 and 1536 °C. The degree of undercooling was assessed by examining the range of temperature where the sample was still liquid, which was down to 1504 °C. Staying above the solidus, this shows a low potential for undercooling with this material in terms of material density. Figure 5(b) displays the density trend developed from 8950 sampling points within the liquid and solid regions of the material from 1100 to 1687 °C. These trends are accompanied by characteristic equations that define the relationship between density and temperature over each respective region. Both equations hold a similar slope, showing the same potential for the expansion of the material at elevated temperatures both above and below the phase transitional zone. In addition, the material exhibited characteristics that show a low potential for rapid material shrinkage, which is often associated with cracking during rapid solidification processes. The main characteristic that points to this implication is the decreased range in between the solid and liquid densities at only a 0.8% difference in value at the solidification temperature.

V. CONCLUSION

In conclusion, we have demonstrated a unique technique that offers significant advantages over a typical AD-XRD setup. By employing an energy-dispersive method for diffraction, many of the disadvantages associated with AD-XRD are eliminated. ED-XRD enables much quicker acquisition times while maintaining a stable experimental setup. This stability facilitates the introduction of novel interaction methods with the sample, such as laser heating and electrostatic levitation. ESL allows us to contain the sample in a vacuum environment without any physical contact, thereby avoiding additional background signal or interfacial interactions with the sample when it is heated.

With this energy-dispersive setup, we can simultaneously determine the structural and compositional stability of a metal alloy at high temperatures. We have demonstrated the capabilities of this experimental setup by observing the martensitic phase transition in Ti–6Al–4V. In addition, we have demonstrated the structural stability alongside the compositional instability of the novel alloy $Ni_{51}Cu_{44}Cr_5$ as well as its density measurement. As new complex concentrated alloys with unique properties are developed for AM processes, this experimental setup can provide valuable insights into the composition–processing–structure–properties of these alloys.

SUPPLEMENTARY MATERIAL

The supplementary material includes details on the energy and angle calibration procedures and fitting programs used to obtain lattice spacing measurements.

03 April 2025 13:33:43

Published under an exclusive license by AIP Publishing

ACKNOWLEDGMENTS

The authors thank the CAMD staff, especially Kevin Morris, for help in commissioning the beamline and generation of simulated incoming x-ray spectrum. We also acknowledge the NASA Marshal Space Flight Center for their loan of the ESL and thank Brandon Phillips, Glenn Fountain, and Brian Hayward for their expertise and support with transporting this equipment. Finally, we thank David Young who synthesized alloy samples used in this study. This work was supported by the National Aeronautics and Space Administration under Grants Nos. 80NSSC21M0296 and 80NSSC19M0149. This work was also supported by the U.S. National Science Foundation under Grant No. OIA-1946231 and the Louisiana Board of Regents for the Louisiana Materials Design Alliance (LAMDA).

AUTHOR DECLARATIONS

Conflict of Interest

The authors have no conflicts to disclose.

Author Contributions

Frank McKay: Data curation (equal); Investigation (equal); Writing – original draft (equal); Writing – review & editing (equal). **Kane Bergeron**: Investigation (supporting); Writing – review & editing (supporting). **Amitava Roy**: Conceptualization (equal). **S. Thomas Britt**: Investigation (supporting); Writing – review & editing (supporting). **Michael P. SanSoucie**: Project administration (equal). **Brandon S. Phillips**: Project administration (equal). **Jonathan Raush**: Investigation (supporting); Project administration (lead); Supervision (lead); Writing – review & editing (supporting). **Phillip T. Sprunger**: Investigation (equal); Supervision (equal); Writing – review & editing (equal).

DATA AVAILABILITY

The data that support the findings of this study are available from the corresponding author upon reasonable request.

REFERENCES

[1]W. E. Frazier, "Metal additive manufacturing: A review," J. Mater. Eng. Perform. **23**, 1917–1928 (2014).
[2]Shoujin Sun, Milan Brandt, and M. Easton, "Powder bed fusion processes: An overview," in *Laser Additive Manufacturing: Materials, Design, Technologies, and Applications*, 1st ed. (Woodhead Publishing, 2017), pp. 55–77.
[3]S. Palanivel, H. Sidhar, and R. Mishra, "Friction stir additive manufacturing: Route to high structural performance," JOM **67**, 616–621 (2015).
[4]T. Mukherjee, J. Zuback, A. De, and T. DebRoy, "Printability of alloys for additive manufacturing," Sci. Rep. **6**(1), 19717 (2016).
[5]C. Brice, R. Shenoy, M. Kral, and K. Buchannan, "Precipitation behavior of aluminum alloy 2139 fabricated using additive manufacturing," Mater. Sci. Eng.: A **648**, 9–14 (2015).
[6]P.-F. Paradis, T. Ishikawa, G.-W. Lee, D. Holland-Moritz, J. Brillo, W.-K. Rhim, and J. T. Okada, "Materials properties measurements and particle beam interactions studies using electrostatic levitation," Mater. Sci. Eng., R **76**, 1–53 (2014).
[7]P.-F. Paradis, T. Ishikawa, and S. Yoda, "Non-contact measurement technique of the vapor pressure of liquid and high temperature solid materials," Eur. Phys. J. Appl. Phys. **22**(2), 97–101 (2003).
[8]S. K. Chung, D. B. Thiessen, and W. K. Rhim, "A noncontact measurement technique for the density and thermal expansion coefficient of solid and liquid materials," Rev. Sci. Instrum. **67**(9), 3175–3181 (1996).
[9]R. Bradshaw, M. Warren, J. Rogers, T. Rathz, A. Gangopadhyay, K. Kelton, and R. Hyers, "Containerless measurements of thermophysical properties of $Zr_{54}Ti_8Cu_{20}Al_{10}Ni_8$," Ann. N. Y. Acad. Sci. **1077**(1), 63–74 (2006).
[10]T. Ishikawa, P.-F. Paradis, and S. Yoda, "New sample levitation initiation and imaging techniques for the processing of refractory metals with an electrostatic levitator furnace," Rev. Sci. Instrum. **72**(5), 2490–2495 (2001).
[11]W.-K. Rhim, K. Ohsaka, P.-F. Paradis, and R. E. Spjut, "Noncontact technique for measuring surface tension and viscosity of molten materials using high temperature electrostatic levitation," Rev. Sci. Instrum. **70**(6), 2796–2801 (1999).
[12]J. Feng and K. V. Beard, "Small-amplitude oscillations of electrostatically levitated drops," Proc. R. Soc. London, Ser. A **430**(1878), 133–150 (1990).
[13]T. Ishikawa, P.-F. Paradis, T. Itami, and S. Yoda, "Non-contact thermophysical property measurements of refractory metals using an electrostatic levitator," Meas. Sci. Technol. **16**(2), 443 (2005).
[14]T. Ishikawa, P.-F. Paradis, J. T. Okada, and Y. Watanabe, "Viscosity measurements of molten refractory metals using an electrostatic levitator," Meas. Sci. Technol. **23**(2), 025305 (2012).
[15]W.-K. Rhim and T. Ishikawa, "Noncontact electrical resistivity measurement technique for molten metals," Rev. Sci. Instrum. **69**(10), 3628–3633 (1998).
[16]G. Rustan, N. Spyrison, A. Kreyssig, R. Prozorov, and A. Goldman, "Noncontact technique for measuring the electrical resistivity and magnetic susceptibility of electrostatically levitated materials," Rev. Sci. Instrum. **83**(10), 103907 (2012).
[17]A. Gangopadhyay, G. Lee, K. Kelton, J. Rogers, A. Goldman, D. Robinson, T. Rathz, and R. Hyers, "Beamline electrostatic levitator for *in situ* high energy x-ray diffraction studies of levitated solids and liquids," Rev. Sci. Instrum. **76**(7), 073901 (2005).
[18]N. Mauro and K. Kelton, "A highly modular beamline electrostatic levitation facility, optimized for *in situ* high-energy x-ray scattering studies of equilibrium and supercooled liquids," Rev. Sci. Instrum. **82**(3), 035114 (2011).
[19]S. Wei, F. Yang, J. Bednarcik, I. Kaban, O. Shuleshova, A. Meyer, and R. Busch, "Liquid–liquid transition in a strong bulk metallic glass-forming liquid," Nat. Commun. **4**(1), 2083 (2013).
[20]D. Holland-Moritz, B. Nowak, F. Yang, and A. Meyer, "Structure and dynamics of glass-forming alloy melts investigated by application of levitation techniques," Pure Appl. Chem. **91**(6), 895–910 (2019).
[21]T. Kordel, D. Holland-Moritz, F. Yang, J. Peters, T. Unruh, T. Hansen, and A. Meyer, "Neutron scattering experiments on liquid droplets using electrostatic levitation," Phys. Rev. B **83**(10), 104205 (2011).
[22]H. Aoki, P.-F. Paradis, T. Ishikawa, T. Aoyama, T. Masaki, S. Yoda, Y. Ishii, and T. Itami, "Development of an electrostatic levitator for neutron diffraction structure analysis," Rev. Sci. Instrum. **74**(2), 1147–1149 (2003).
[23]R. Caminiti and V. R. Albertini, "The kinetics of phase transitions observed by energy-dispersive X-ray diffraction," Int. Rev. Phys. Chem. **18**(2), 263–299 (1999).
[24]J. Rogers and M. Sansoucie, "Containerless processing studies in the MSFC electrostatic levitator," in *50th AIAA Aerospace Sciences Meeting Including the New Horizons Forum and Aerospace Exposition,* (Aerospace Research Central, 2012), p. 924.
[25]T. Egami, "Structural relaxation in amorphous $Fe_{40}Ni_{40}P_{14}B_6$ studied by energy dispersive X-ray diffraction," J. Mater. Sci. **13**(12), 2587–2599 (1978).
[26]K. Nishikawa and T. Iijima, "Corrections for intensity data in energy-dispersive X-ray diffractometry of liquids. Application to carbon tetrachloride," Bull. Chem. Soc. Jpn. **57**(7), 1750–1759 (1984).
[27]A. C. Marschilok, A. M. Bruck, A. Abraham, C. A. Stackhouse, K. J. Takeuchi, E. S. Takeuchi, M. Croft, and J. W. Gallaway, "Energy dispersive X-ray diffraction (EDXRD) for operando materials characterization within batteries," Phys. Chem. Chem. Phys. **22**(37), 20972–20989 (2020).
[28]A. C. Thompson and D. Vaughan, *X-Ray Data Booklet* (Lawrence Berkeley National Laboratory, University of California, Berkeley, CA, 2001).

03 April 2025 13:33:43

Published under an exclusive license by AIP Publishing

[29]B. L. Henke, E. M. Gullikson, and J. C. Davis, "X-ray interactions: Photoabsorption, scattering, transmission, and reflection at E = 50–30,000 eV, Z = 1–92," At. Data Nucl. Data Tables **54**(2), 181–342 (1993).
[30]M. S. del Río and R. J. Dejus, "Xop v2. 4: Recent developments of the x-ray optics software toolkit," in *Advances in Computational Methods for X-Ray Optics II*, 8141 (SPIE Digital Library, 2011), pp. 368–372.
[31]C. Khan Malek, V. Saile, H. Manohara, and B. Craft, "Deep X-ray lithography with a tunable wavelength shifter at CAMD," J. Synchrotron Radiat. **5**(3), 1095–1098 (1998).
[32]Y. Lee and D. Farson, "Surface tension-powered build dimension control in laser additive manufacturing process," Int. J. Adv. Des. Manuf. Technol. **85**, 1035–1044 (2016).
[33]J. Coleman, A. Plotkowski, B. Stump, N. Raghavan, A. Sabau, M. Krane, J. Heigel, R. Ricker, L. Levine, and S. Babu, "Sensitivity of thermal predictions to uncertain surface tension data in laser additive manufacturing," J. Heat Transfer **142**(12), 122201 (2020).
[34]A. J. Rulison, J. L. Watkins, and B. Zambrano, "Electrostatic containerless processing system," Rev. Sci. Instrum. **68**(7), 2856–2863 (1997).
[35]J. Nawer, X. Xiao, M. SanSoucie, and D. Matson, "Effect of mass evaporation on measurement of liquid density of Ni-based superalloys using ground and space levitation techniques," High Temp. - High Pressures **49**, 17–29 (2020).
[36]J. Lee and D. Matson, "Prediction of mass evaporation of $Fe_{50}Co_{50}$ during measurements of thermophysical properties using an electrostatic levitator," Int. J. Thermophys. **35**, 1697–1704 (2014).
[37]F. Wang, S. Williams, P. Colegrove, and A. A. Antonysamy, "Microstructure and mechanical properties of wire and arc additive manufactured Ti–6Al–4V," Metall. Mater. Trans. A **44**, 968–977 (2013).
[38]S. Kelly and S. Kampe, "Microstructural evolution in laser-deposited multilayer Ti–6Al–4V builds: Part I. Microstructural characterization," Metall. Mater. Trans. A **35**, 1861–1867 (2004).
[39]J.-O. Andersson, T. Helander, L. Höglund, P. Shi, and B. Sundman, "Thermo-Calc & DICTRA, computational tools for materials science," Calphad **26**(2), 273–312 (2002).
[40]G. Welsch, R. Boyer, and E. Collings, *Materials Properties Handbook: Titanium Alloys* (ASM International, 1993).
[41]M. J. Donachie, *Titanium: A Technical Guide* (ASM International, 2000).
[42]A. Zadi-Maad and A. Basuki, "The development of additive manufacturing technique for nickel-base alloys: A review," AIP Conf. Proc. **1945**, 020064 (2018).
[43]A. Vahedi Nemani, M. Ghaffari, K. Sabet Bokati, N. Valizade, E. Afshari, and A. Nasiri, "Advancements in additive manufacturing for copper-based alloys and composites: A comprehensive review," J. Manuf. Mater. Process. **8**(2), 54 (2024).
[44]E. Mack, G. G. Osterhof, and H. M. Kraner, "Vapor pressure of copper oxide and of copper," J. Am. Chem. Soc. **45**(3), 617–623 (1923).
[45]H. Johnston and A. Marshall, "Vapor pressures of nickel and of nickel oxide," J. Am. Chem. Soc. **62**(6), 1382–1390 (1940).
[46]L. Vegard, "Die Konstitution der Mischkristalle und die Raumfüllung der Atome," Z. Phys. **5**(1), 17–26 (1921).
[47]A. R. Denton and N. W. Ashcroft, "Vegard's law," Phys. Rev. A **43**(6), 3161 (1991).
[48]S. Murphy, A. Chroneos, C. Jiang, U. Schwingenschlögl, and R. Grimes, "Deviations from Vegard's law in ternary III–V alloys," Phys. Rev. B **82**(7), 073201 (2010).
[49]H. E. Swanson, *Standard X-Ray Diffraction Powder Patterns* (US Department of Commerce, National Bureau of Standards, 1970).

03 April 2025 13:33:43

Published under an exclusive license by AIP Publishing